Materials Advances

ROYAL SOCIETY OF CHEMISTRY

PAPER

View Article Online
View Journal | View Issue

Cite this: *Mater. Adv.*, 2025, **6**, 6370

CuBTC–clay composites with tunable ratios for antibiotic removal: unraveling isotherm, kinetic, and thermodynamic study†

Palkaran Sethi,[a] Sanghamitra Barman *[b] and Soumen Basu *[a]

The growing contamination of water bodies with persistent antibiotics, such as tetracycline, presents a critical environmental challenge, demanding urgent and effective remediation strategies. The present investigation introduces a novel adsorbent, a hybrid composite of CuBTC and HNT clay, engineered for the highly efficient removal of tetracycline (TC) from wastewater. The CuBTC–HNT composite was synthesized in different ratios (1 : 1, 1 : 3, 3 : 1, and 1 : 5) and underwent extensive characterization using FESEM, EDS, FTIR, XPS, XRD, HRTEM, TGA, and BET surface area analysis. The adsorption process was carefully optimised using the synthesised hybrid composite as an adsorbent by adjusting crucial variables like dose, contaminant concentration, pH, temperature, stirring speed, and contact duration. Under optimized conditions, the composite demonstrated an outstanding adsorption efficiency of 94% of 25 ppm TC in 35 minutes within the pH range of 5–10. Moreover, reusability tests showed a consistent adsorption performance of 82% even after multiple cycles, reinforcing its sustainability and practical feasibility. Six different equilibrium isotherm models were employed: Freundlich, Temkin, Harkins–Jura, Halsey, Dubinin-Radushkevich, and Langmuir. Among these, the Langmuir model showed the best fit with a high correlation coefficient (R^2 = 0.9963), confirming monolayer adsorption primarily governed by physiosorption (adsorption energy: 6.13 kJ mol^{-1}). Mechanistic insights from after-adsorption characterization (XRD, FTIR, and FESEM-EDS) revealed key interactions, including π–π stacking, hydrogen bonding, electrostatic attractions, and pore filling. Kinetic studies were conducted using five models—pseudo-first-order, pseudo-second-order, elovich, intraparticle diffusion, and liquid film model—where the pseudo-second-order model best described the adsorption process (R^2 = 0.997), while thermodynamic analysis indicated that the process was endothermic, spontaneous, and entropically favourable (ΔH = 34.73423 kJ mol^{-1}, ΔG = −0.49777 kJ mol^{-1}, and ΔS = 0.109077 kJ mol^{-1} K^{-1}). This research delivers a comprehensive and in-depth evaluation of an advanced adsorption system, bridging fundamental adsorption science with practical environmental applications which is an urgent global need for cleaner and safer water resources.

Received 13th June 2025,
Accepted 23rd July 2025

DOI: 10.1039/d5ma00639b

rsc.li/materials-advances

1. Introduction

Imagine a world where the water we drink carries traces of the antibiotics meant to cure diseases, silently fuelling the rise of superbugs. This is no longer a hypothetical scenario but a growing global reality. The unchecked discharge of pharmaceutical pollutants, particularly antibiotics like tetracycline (TC), has become a critical environmental challenge.[1] Elevated concentrations of TC pose severe toxic risks, hindering the proliferation and activity of microorganisms, plants, and animals. This alarming scenario underscores the urgent necessity for innovative technologies to eliminate antibiotics from environmental systems effectively.[2,3] A range of strategies, including photolysis,[4] hydrolysis,[5] thermolysis,[6] adsorption, and catalytic oxidation,[7] have been explored to address antibiotic contamination. However, these methods, predominantly reliant on chemical treatments, often face challenges such as limited adsorption efficiency, high energy demands, and poor selectivity. Moreover, chemical degradation processes carry the risk of generating secondary pollutants, further complicating their environmental impact.[8] Adsorption stands out as the most effective solution, offering unmatched affordability, ease of use, and versatility, coupled with a simple yet efficient design that ensures reliable removal of contaminants.[9] A diverse range

---

[a] *Department of Chemistry and Biochemistry, Thapar Institute of Engineering and Technology, Patiala-147004, Punjab, India. E-mail: soumen.basu@thapar.edu*
[b] *Department of Chemical Engineering, Thapar Institute of Engineering and Technology, Patiala-147004, Punjab, India. E-mail: sbarman@thapar.edu*

† Electronic supplementary information (ESI) available. See DOI: **https://doi.org/10.1039/d5ma00639b**

of materials, such as minerals, resins, activated carbon, silica, polymers, metal oxides, and charcoal, have been utilized as adsorbents for antibiotic removal.[10] Despite their widespread use, existing adsorbents suffer from significant limitations. For instance, producing activated carbon is energy-intensive and costly, while many adsorbents show low reusability, slow adsorption kinetics, and limited efficiency in pollutant removal. Some even generate unwanted by-products or require high dosages to be effective. To address these challenges, this study explores a novel and efficient coordination polymer-based adsorbent specifically designed to remove antibiotics from wastewater.[11,12] Coordination polymers (CPs) and metal–organic frameworks (MOFs) are hybrid materials formed by the interplay of metal ions and organic ligands,[13] offering tunable pore sizes, large surface areas, and exceptional stability. Their versatility makes them ideal for applications like sensing, catalysis, and adsorption. Among different CPs, CuBTC (HKUST-1) (CB), a well-known coordination polymer, was selected for its high surface area, permanent porosity, open metal sites, and strong affinity toward polar and aromatic molecules, including tetracycline *via* π–π interactions, hydrogen bonding, and coordination mechanisms.[14] However, its practical applications are hindered by inherent limitations such as poor water stability, structural fragility, and agglomeration tendencies in aqueous environments.[15] To address these challenges, researchers have focused on fabricating CB-based composites by integrating it with complementary materials that enhance their performance.[16,17] Clay minerals have garnered considerable interest for this purpose due to their low cost, eco-friendliness, abundance, and excellent physicochemical properties. They possess strong cation exchange capacities and moderate surface areas, which, when modified to nano-forms, exhibit significantly improved adsorption performance. Halloysite nanotubes (HN), a biocompatible clay mineral, possess a unique tubular morphology, large specific surface area, robust mechanical stability, and diverse surface functionalities. These properties make them ideal candidates for composite fabrication with CPs. HN can reinforce the structural integrity of CB, improve its dispersion, and enhance its reusability. By incorporating HN into CB, synergistic effects are achieved that lead to increased adsorption efficiency and stability under aqueous conditions.[18,19]

For instance, an HNT–Fe_3O_4 composite with a remarkable surface area was developed for the efficient adsorption of tetracycline. This composite demonstrated superior adsorption capacity, following pseudo-second-order kinetics, and retained structural stability over multiple regeneration cycles, showcasing its potential for antibiotic removal from wastewater.[20] Another previous study explored the use of the HNTs/GO composite for the adsorption of fluoroquinolone antibiotics such as levofloxacin and ciprofloxacin across a broad pH spectrum.[21] Also, two different CuBTC-based composites have demonstrated excellent adsorption capabilities for pollutant removal. A CuBTC/PANI composite effectively adsorbed Reactive Blue-19 dye with 99% efficiency at pH 2, while a CuBTC/GO composite achieved 97.7% tetracycline removal at pH 10. Both systems showcased CuBTC's versatility in adsorptive applications.[15,22]

While numerous composite materials have shown promise for antibiotic removal, a tailored solution for tetracycline with enhanced stability, faster kinetics, a wide pH working range, and reusability remains elusive. This study bridges that gap by introducing a novel CuBTC–HNT (CH) composite synthesized in varying ratios, specifically designed for efficient TC adsorption. A critical research gap addressed here is the unexplored potential of CH composites for antibiotic adsorption, especially for tetracycline, despite their complementary properties. Additionally, the effect of varying CB : HN ratios (1 : 1, 1 : 3, 3 : 1, and 1 : 5) on the adsorption efficiency was systematically studied to identify the optimal combination for maximum performance. This compositional tuning aimed to systematically investigate the impact of component proportion on key physicochemical parameters, including surface area, porosity, and structural stability. The primary contribution of this study lies in the fabrication and thorough investigation of a CH hybrid composite for tetracycline adsorption, which provides insights into its structural, thermal, and functional properties. The material's structural and functional characteristics were validated through an array of analytical techniques, including BET, XPS, TGA, HRTEM, FTIR, EDS, FESEM, and XRD. A comprehensive assessment of adsorption performance was performed by varying key operational factors like pH, contact duration, adsorbent amount, aggitation rate, temperature, and adsorbate concentration. Additionally, adsorption kinetics, equilibrium isotherms, and thermodynamic parameters (ΔH°, ΔS°, and ΔG°) were thoroughly examined. A proposed adsorption mechanism sheds light on the process, positioning this composite as a cutting-edge solution for tackling emerging pollutants in wastewater treatment.

2. Experimental materials

Materials used in the synthesis are listed in section S1, ESI.†

2.1. Synthesis of the CuBTC/HNT composite

CuBTC was synthesized using a previously reported method, as described in our earlier work[15] and HN clay was used as purchased. Then the CuBTC/HNT composite was synthesised by sonicating a suspension of halloysite nanotube clay in a 50 : 50 ethanol–water combination for an hour. Separately, $Cu(NO_3)_2\cdot 3H_2O$ (0.358 g, 1.5 mmol) and trimesic acid (0.211 g, 1 mmol) were dissolved in a 12 mL ethanol–water mixture to form a solution. The prepared solution was added to the HNT suspension, followed by vigorous sonication for 15 minutes to achieve homogeneous dispersion. After that, the mixture was moved to an autoclave lined with Teflon, heated for 24 hours at 110 °C, and cooled to ambient temperature. The obtained CuBTC/HNT hybrid materials were sonicated in an ethanol–water mixture for 15 minutes, then separated by filtration and left to air-dry for 24 hours. Four composites—CH11, CH13, CH15, and CH31—were synthesized by varying the CuBTC-to-HNT ratios to 1 : 1, 1 : 3, 1 : 5, and 3 : 1, respectively (Scheme 1).

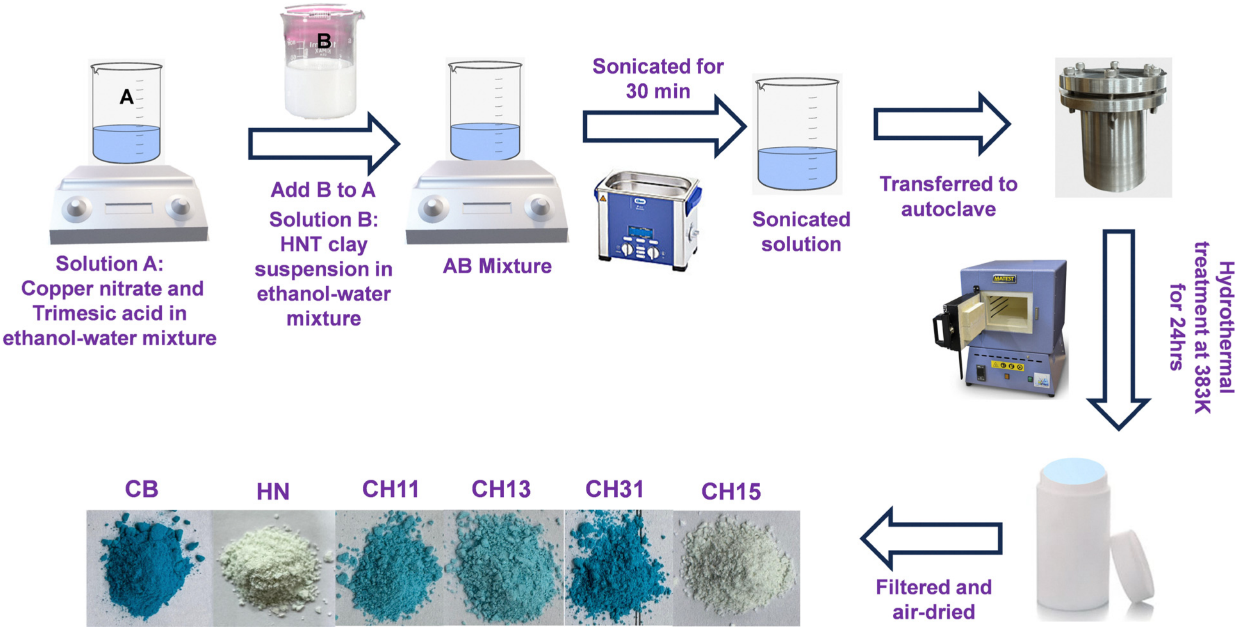

Scheme 1 Graphical illustration of step-by-step synthesis of CH composites.

2.2. Characterisation methods

Detailed descriptions of the characterization methods and instruments utilized can be found in section S2, ESI.†

2.3. Adsorption experiments

Detailed description of adsorption experiments can be found in section S3, ESI.†

3. Results and discussion

3.1. Adsorbent characterisation

3.1.1. XRD spectra. The CB, HN, CH11, CH13, CH31, and CH15 composites' crystalline structure and purity are confirmed using the XRD pattern shown in Fig. 1(a). Peaks observed at 2θ values of 6.7° (200), 9.52° (220), 11.64° (222), 13.44° (440), 14.96° (422), 17.48° (511), 19.03° (440), 20.20° (660), 25.82° (730), 29.28° (751), 35.86° (773), 39.17° (828), and 47.16° (751) confirm the successful formation of CB, highlighting its well-defined crystalline framework.[23] The XRD spectra of HN were analyzed with well-defined diffraction peaks observed at 2θ values of 12.2° (001), 20.1° (100), 25.1° (002), 34.9° (110), 37.9° (003), 54.5° (210), and 62.4° (300), confirming the crystalline nature of HN. The (001) peak at 2θ = 12.2° was identified, indicating an interlayer spacing of 0.73 nm, characteristic of halloysite with a 7 Å layer structure.[24] The XRD analysis of the composites revealed peaks corresponding to both CB and HN, with the slight peak shifts observed in the composite materials likely indicating lattice

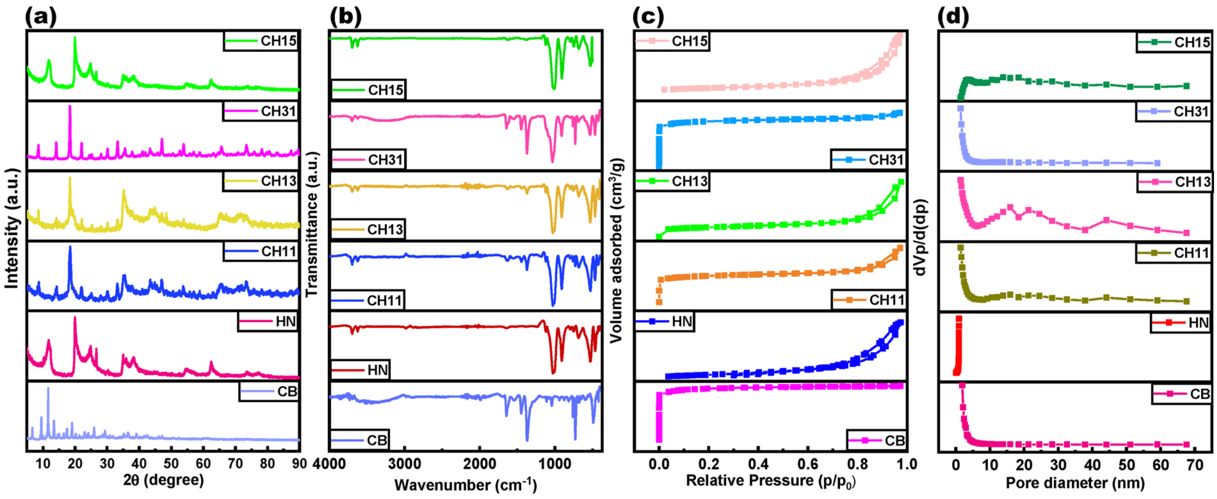

Fig. 1 (a) XRD profiles, (b) FTIR plots, (c) BET plots, and (d) BJH curves of CB, HN, CH11, CH13, CH31, and CH15.

distortion or interfacial interaction between CB and HN. This can result from partial intercalation, chemical bonding, or strain introduced during synthesis, causing minor changes in interlayer spacing. The absence of any additional peaks further verified the purity of the synthesized materials. Additionally, variations in peak intensities were observed in the hybrid composites (CH11, CH13, CH31, and CH15), reflecting the influence of the relative concentrations of CB and HN in the composite structure. This confirms the effective integration of the two components across different ratios. Some peaks in the composite spectra may result from overlapping diffraction planes of CB and HN, especially where their 2θ values are close.

3.1.2. FTIR spectra. The FTIR spectra of the bare CB, HN and the composites CH11, CH13, CH31, and CH15 are shown in Fig. 1(b), confirming the presence of various functional groups. CB exhibits characteristic FTIR peaks at 3447 cm^{-1} corresponding to O–H stretching vibrations from coordinated or adsorbed water. Peaks at 1691 cm^{-1} and 1525 cm^{-1} indicate the presence of coordinated or free carboxylate (–COO^{-}) groups, essential components in BTC-based metal–organic frameworks. Additionally, the peak at 1637 cm^{-1} is attributed to C═O stretching, while the bands at 1446 cm^{-1} and 1373 cm^{-1} correspond to the asymmetric and symmetric stretching vibrations of the BTC carboxylate groups, respectively. The 1111 cm^{-1} band corresponds to the C–O–Cu vibration, confirming the coordination between BTC ligands and copper ions in the framework. The benzene ring's out-of-plane C–H bending vibrations are identified at 759 and 727 cm^{-1}.[25] For HNT, peaks at 903 cm^{-1} and 3694 cm^{-1} confirm Al–O–OH bending and O–H stretching, while in-plane Si–O–Si vibrations appear at 1115 cm^{-1} and 1030 cm^{-1} suggesting a typical layered aluminosilicate structure with reactive hydroxyl groups.[24] The nanocomposite's spectra exhibit similar peaks with minor shifting corresponding to these functional groups, indicating the successful synthesis.

3.1.3. BET evaluation. A BET analyser was employed to evaluate the surface area, pore volume, and pore size distribution of CB, HN, and the composites (Fig. 1(c), and Table 1). CB and the CH31 are microporous materials and exhibit a reversible Type I isotherm, providing a large surface area that is perfect for adsorbing tiny molecules. In contrast, HN, CH11, CH13, and CH15 are mesoporous, showing Type IV isotherms with noticeable hysteresis loops, which confirm capillary condensation and suggest good accessibility and diffusion pathways for larger molecules, both of which are crucial for efficient contaminant diffusion and adsorption. The incorporation of mesoporous HN into microporous CB leads to a hybrid pore structure, combining micropores and mesopores. This improves the overall pore volume and adsorption efficiency, especially for larger or complex contaminants. Also, BJH analysis in Fig. 1(d) revealed that CB and the composite predominantly possess micropores (<2 nm), while HN, CH11, CH13, and CH15 feature mesopores (2–50 nm). Incorporating HN into CB enhanced the pore size and introduced mesoporosity, significantly boosting the composite's adsorption removal. This improvement in pore structure facilitates faster intraparticle diffusion and enhanced accessibility of active sites, thereby contributing to superior adsorption kinetics and overall efficiency, particularly in the case of bulky antibiotic molecules. This combination effectively combines the microporous and mesoporous advantages, optimizing pollutant removal efficiency.[26]

Table 1 Surface area, total pore capacity, and average pore size analysis

Adsorbent (CuBTC : HNT)	Surface area (m^2 g^{-1})	Total pore capacity (cm^3 g^{-1})	Average pore size (nm)
CB (1 : 0)	1223.2	0.5032	1.6456
HN (0 : 1)	43.093	0.1696	15.742
CH11 (1 : 1)	354.91	0.2576	2.9028
CH13 (1 : 3)	154.9	0.1991	18.849
CH31 (3 : 1)	941.35	0.4393	1.8667
CH15 (1 : 5)	41.211	0.1942	5.1421

3.1.4. XPS spectra. X-ray photoelectron spectroscopy (XPS) identifies surface functional groups, oxidation states, and elemental composition, all of which directly influence adsorption efficiency by controlling interaction sites, charge distribution, and chemical compatibility with adsorbates. This technique enables the detection of spin–orbit splitting in metal ions, which appears as two distinct states, each characterized by specific binding energies. The survey scan verified the existence of elements—C, O, Cu, Al, and Si—originating from both CB and HN components (Fig. 2(a)). The spectral deconvolution was performed using a least-squares Gaussian fitting method. Prominent peaks in the Cu 2p spectra were seen in Fig. 2(b) at roughly 933.5 eV and 953.2 eV, which correspond to Cu^{2+} in the Cu 2p$_{3/2}$ and Cu 2p$_{1/2}$ correspondingly. Furthermore, shake-up transitions linked to Cu(II) species are responsible for satellite peaks seen at 937–945 eV and 960–965 eV. A peak at 288.7 eV verified the presence of C═O groups from the BTC ligand, whereas peaks at 284.7 eV and 285.7 eV indicated C–C and C–H bonds in the C 1s spectrum, which is displayed in Fig. 2(c). Fig. 2(d) shows the deconvoluted O 1s spectrum, revealing two distinct peaks at 532.2 eV and 531.2 eV, corresponding to surface-adsorbed oxygen and moisture linked to the BTC and HNT structures. Fig. 2(e) shows Si 2p peaks at 101.47 and 103.62 eV (Si–O), while Fig. 2(f) displays Al 2p peaks at 74.88 and 75.1 eV (Al–O in HNT).[27,28] These findings confirm the successful integration of CB and HN into the CH13 composite and validate its structural and chemical integrity, which is essential for its effective adsorption performance.

3.1.5. TGA spectra. TGA was performed under nitrogen to assess the thermal stability of CB, HN, and CH13, showing a thermal profile influenced by both components, as illustrated in Fig. S1 (ESI†). The TGA curves exhibited two major weight loss stages; the first (30–200 °C) was due to the removal of physisorbed/interlayer water and volatile residues like ethanol. This stage followed the behavior observed in CB and HN with TGA. CB exhibits higher weight loss due to its lower stability during this phase. The second stage (200–550 °C) corresponded to HN dehydroxylation and CB decomposition, with peak weight loss around 330 °C for CB. Importantly, the CH13 composite demonstrated enhanced thermal stability compared to pure CB, attributable to the incorporation of HN. This integration improved the structural robustness and reduced the decomposition

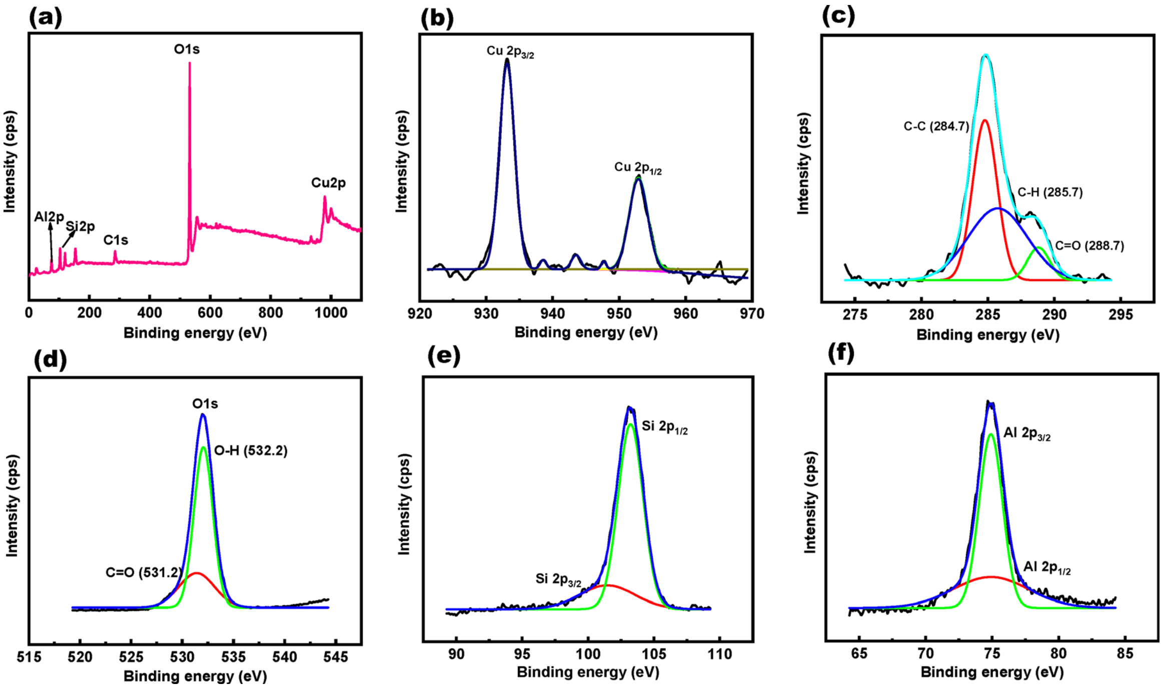

Fig. 2 XPS spectra of CH13: (a) survey scan, (b) Cu 2p, (c) C 1s, (d) O 1s, (e) Si 2p, and (f) Al 2p core levels.

rate of CB, making the composite more thermally stable and suitable for advanced applications.

3.1.6. FESEM-EDS mapping and HRTEM analysis. The structural characteristics of the synthesized CB, HN, and their composite were investigated using FESEM. As shown in Fig. 3(a–c), the FESEM images reveal the distinct morphologies of CB, HN, and the CH13 composites. The octahedral shape of CB suggests a highly crystalline structure, likely derived from its BTC ligand coordination with metal ions. This geometry is characteristic of well-formed CP crystals, contributing to uniform pore distribution and surface area. The tubular structure of HN's increases the surface area and provides internal mesopores, which facilitate better diffusion pathways and enhanced adsorption kinetics, especially for large contaminants. In the composite, both morphologies are seamlessly integrated, showcasing the successful synthesis and the formation of a synergistic hybrid structure. EDS analysis (Fig. 3(d)) confirmed the elemental composition of the composite, highlighting the presence of Cu, C, O, Si, and Al. Additionally, elemental mapping (Fig. 3(e–j)) revealed a uniform distribution of these elements, contributing to the composite's enhanced structural stability and improved adsorption capabilities.

HRTEM was employed to gain deeper insights into the microstructural features and morphology of the CH13 composite. In Fig. 3(k–m), images at varying magnification levels demonstrated the successful integration of CB crystals with the tubular structure of HN. The CB appeared as well-defined polyhedral nanocrystals uniformly distributed along the surface and within the hollow interiors of the HN, confirming strong interfacial interaction between the two components. The lattice fringes observed in the CB regions exhibited interplanar spacings corresponding to the (222) planes, indicative of its crystalline nature. Meanwhile, the tubular morphology of HN remained intact, providing a stable scaffold for CB dispersion. The images showed intimate contact between CB and HN, which support the formation of a stable hybrid architecture, which contributes to the overall adsorption performance of the composite. These findings validate the synergistic structure of the CH13 composite and its suitability for efficient TC adsorption.

3.2. Impact of CB and HN ratios on TC adsorption efficiency

The effect of varying ratios of CB and HN in the composite was studied to optimize the adsorptive removal of TC (Fig. 4(a)). Composites with CB : HN ratios of 1 : 1, 1 : 3, and 3 : 1 were initially synthesized, yielding removal efficiencies of 63.9%, 75.1%, and 47.6%, respectively. The 1 : 3 ratio demonstrated the highest efficiency, indicating an optimal balance between the properties of CB and HN. To further explore this trend, a composite with a 1 : 5 ratio was synthesized, but the removal efficiency decreased to 60.9%. This reduction suggests that an excessive HNT content negatively impacts the adsorption performance, likely due to diminished contributions from CB's microporous structure. The superior performance of the 1 : 3 composite (CH13) can be attributed to its optimal pore size, which significantly enhances the adsorption of TC by providing an ideal pathway for molecular diffusion and interaction. These findings underscore the importance of tailoring the CB: HN ratio to achieve maximum adsorption efficiency.

3.3. Impact of initial TC concentration on its adsorption efficiency

Fig. 4(b) shows the impact of initial TC concentration on its removal. As the concentration increased from 25 to 50 mg L^{-1},

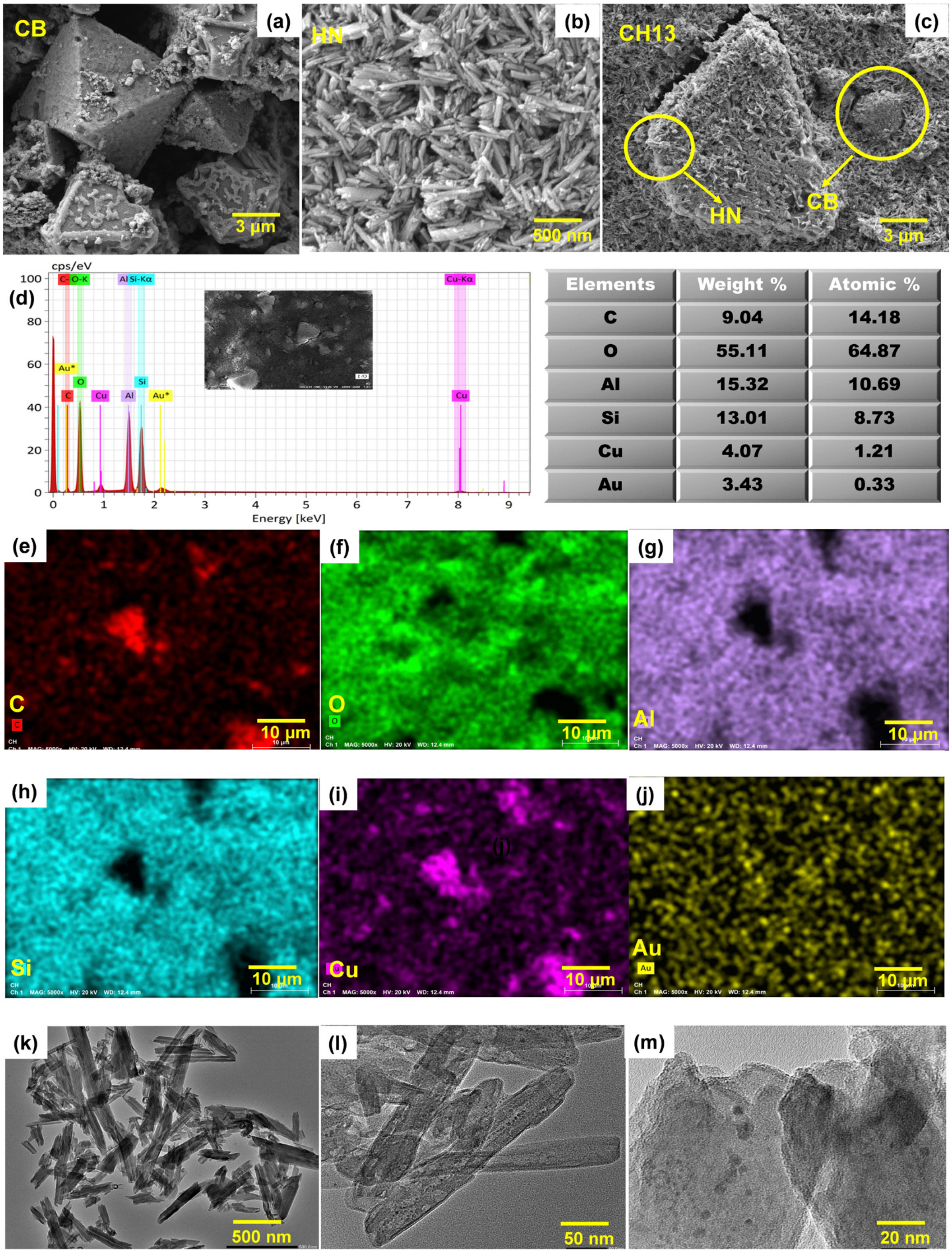

Elements	Weight %	Atomic %
C	9.04	14.18
O	55.11	64.87
Al	15.32	10.69
Si	13.01	8.73
Cu	4.07	1.21
Au	3.43	0.33

Fig. 3 FESEM images of (a) CB, (b) HN, and (c) CH13, (d) EDS spectrum of CH13, (e) and (j) elemental coloured mapping of various elements, and (k)–(m) HRTEM images of CH13 at different magnifications.

the removal efficiency decreased from 78% to 42%. This decrease is due to increased competition among adsorbate molecules for the finite active sites on the composite surface. At higher concentrations, TC molecules tend to aggregate or cluster on the adsorbent surface. This clustering can block access to active sites or alter the surface environment, creating steric hindrance or repulsive interactions that hinder further adsorption, thus reducing overall efficiency. Additionally, when adsorption sites are saturated and solute concentration remains high, a dynamic equilibrium may form, causing some adsorbed molecules to desorb back into the solution, reducing the net adsorption capacity and diminishing the overall removal efficiency.

3.4. Impact of adsorbent dosage on TC adsorption efficiency

As shown in Fig. 4(c), TC removal was enhanced from 44% to 93% with an increase in CH13 dosage from 0.1 g L^{-1} to 0.5 g L^{-1}, at a

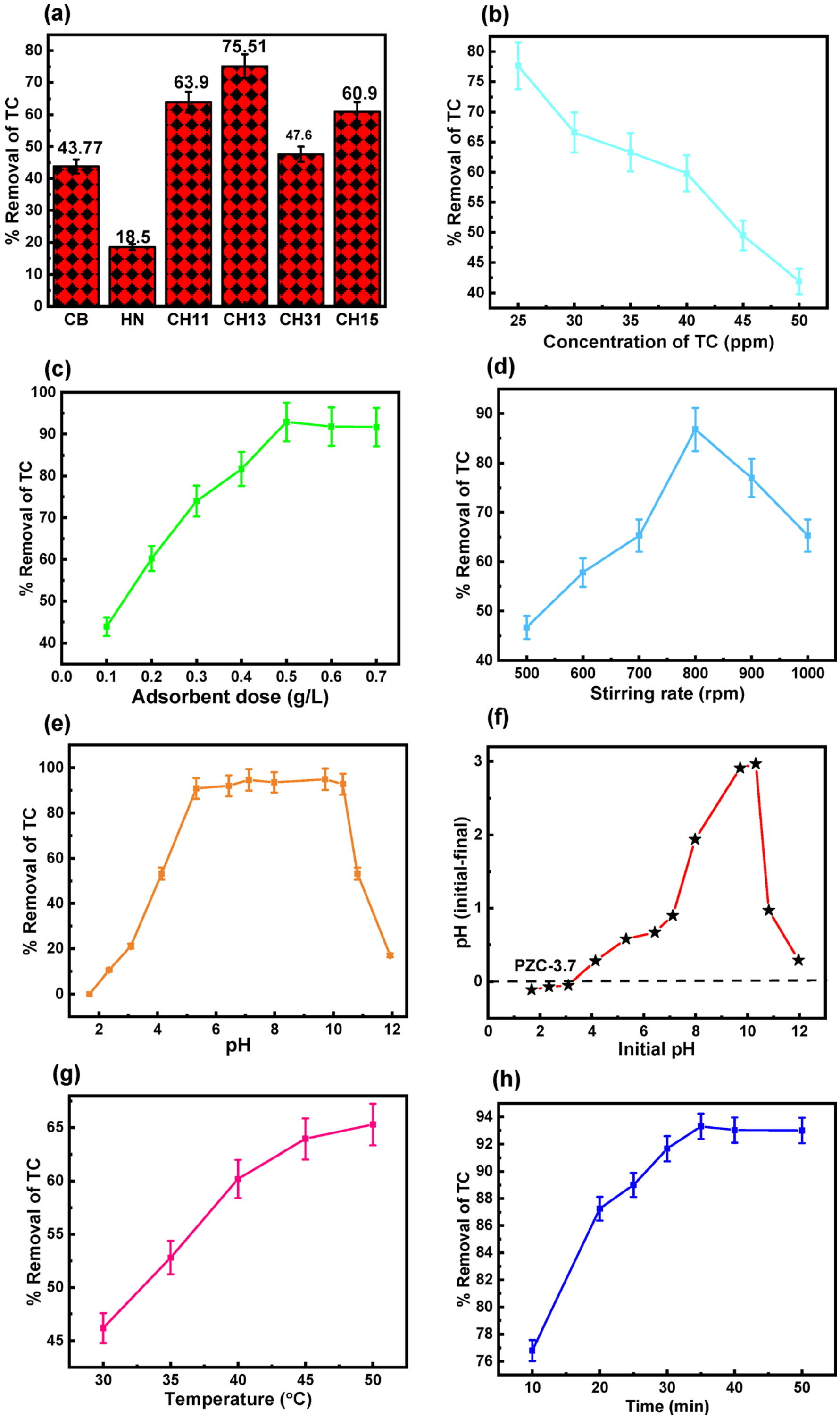

Fig. 4 Impact of (a) different ratios of CB and HN, (b) initial concentration of TC, (c) dosage of the adsorbent, (d) stirring rate, (e) pH, (f) PZC, (g) temperature and (h) time on adsorption efficiency of TC on CH13.

constant TC concentration of 25 mg L^{-1} and a contact time of 50 minutes. However, further increasing the dose to 0.7 g L^{-1} did not yield a noticeable improvement, with removal efficiency remaining nearly constant at 92%. The improved adsorption at higher doses (up to 0.5 g L^{-1}) is due to the greater number of available active sites, allowing more TC molecules to bind effectively. Beyond this point, the adsorption process reaches saturation, where most of the adsorbate molecules are already adsorbed, and additional adsorbent contributes minimally to removal. Factors like limited adsorbate availability, particle agglomeration, and equilibrium saturation further explain the observed constancy at higher doses.[29]

3.5. Impact of agitation rate on TC adsorption efficiency

The impact of agitation rate on TC removal was explored using 0.5 g L^{-1} of CH13 and a TC concentration of 25 mg L^{-1}. As shown in Fig. 4(d), the removal efficiency increased steadily with stirring speed, peaking at 87% at 800 rpm. This improvement results from better mass transfer, increasing TC molecule interaction with CH13 active sites. Moreover, increased stirring speeds decrease the boundary layer thickness around adsorbent particles, enhancing access to active sites. However, when the stirring speed exceeded 800 rpm, the removal efficiency began to decline. This decrease is likely due to excessive turbulence in the system, causing particles to collide and aggregate. The clustering diminishes the surface area and obstructs access to active sites, resulting in reduced adsorption efficiency.

3.6. Impact of solution's pH on TC adsorption efficiency

As shown in Fig. 4(e), the adsorption of TC by the CH13 was investigated throughout a wide pH range from 1 to 12. This range was chosen to evaluate the adsorbent's performance under both highly acidic and basic conditions. The findings revealed that the adsorption increased significantly from pH 4 and stabilized at approximately 94% between pH 5 and 10. Beyond pH 10, a slight decline in adsorption was observed. The adsorption behavior is closely linked to the experimentally determined point of zero charge (PZC) of the adsorbent using the pH drift method around 3.7 (Fig. 4(f)). At pH values below the PZC, the adsorbent surface carries positive charge, resulting in electrostatic repulsion with the cationic forms of TC, leading to lower adsorption. At pH levels above the PZC, the surface becomes negatively charged, and TC exists predominantly in its zwitterionic or anionic forms,[30,31] facilitating π–π stacking interactions, hydrogen bonding, and strong electrostatic attractions. The stable adsorption efficiency observed between pH 5 and 10 suggests that the adsorbent's performance is robust and less sensitive to pH variations in this range. The decrease in adsorption efficiency beyond pH 10 is owing to the repulsion from the negatively charged adsorbent surface and deprotonated tetracycline species, reducing their interaction. This stability, coupled with high removal efficiency, highlights the adsorbent's suitability for practical applications in wastewater treatment over a wide pH spectrum.

3.7. Impact of temperature on TC adsorption efficiency

The effect of temperature on the adsorption process was explored by conducting experiments at temperatures ranging from 30 °C to 50 °C, with all other parameters held constant. As depicted in Fig. 4(g), the adsorption efficiency consistently improved with increasing temperature, demonstrating the endothermic nature of the process. This increase can be explained by the enhanced kinetic energy of TC molecules at higher temperatures, which promotes better contact with the adsorbent's active sites. Additionally, elevated temperatures may activate the adsorbent, exposing more active sites and improving its overall capacity. These findings emphasize the favorable thermodynamic nature of the process at elevated temperatures, making it highly effective within the studied range. Higher temperature studies were not conducted because adsorption efficiency was highest at 50 °C. Exploring temperatures above 50 °C was deemed impracticable because wastewater treatment typically takes place at low temperatures. These findings highlight the suitability of the adsorbent for real-world scenarios within this temperature range.

3.8. Impact of time on TC adsorption efficiency

Contact time's effect on TC's adsorption onto CH13 was assessed throughout a range of time periods (0–50 min). As depicted in Fig. 4(h), the percentage of TC removed increased significantly during the initial phase, rising from 77% to 93.3% within the first 35 minutes. The adsorbent surface's large number of active sites causes this quick adsorption. Beyond 35 minutes, the removal efficiency plateaued, indicating that adsorption equilibrium had been achieved and the adsorbate molecules had saturated the active sites. Thus, 35 minutes was found to be the ideal contact period for maximal adsorption.

3.9. Adsorption isotherms

Adsorption isotherms are essential for analyzing the equilibrium interaction between TC and the surface of CH13, revealing adsorption capacity, mechanism, and interaction type. In this study, Langmuir, Freundlich, Temkin, Halsey, Harkins–Jura, and Dubinin-Radushkevich isotherms were analysed to evaluate the adsorption behaviour and efficiency comprehensively.

The linearized forms of the adsorption isotherms are presented below. These isotherm models' fit and dependability were assessed using the Pearson correlation coefficient (R^2).

Langmuir isotherm:

$$\frac{C_e}{q_e} = \frac{1}{Q_m K_L} + \frac{1}{Q_m} C_e \tag{1}$$

$$R_L = \frac{1}{1 + K_L C_0} \tag{2}$$

Freundlich isotherm:

$$\log q_e = \log K_f + \frac{\log C_e}{n} \tag{3}$$

Halsey isotherm:

$$\ln q_e = \frac{1}{n} \ln K - \frac{1}{n} \ln C_e \tag{4}$$

Harkins–Jura isotherm:

$$\frac{1}{{q_e}^2} = \left(\frac{B}{A}\right) - \frac{1}{A} \log C_e \tag{5}$$

Temkin isotherm:

$$q_e = B_T \ln K_T + B_T \ln C_e \tag{6}$$

Dubinin–Radushkevich model:

$$\ln q_{\mathrm{e}} = \ln Q_{\mathrm{s}} + B\varepsilon^2 \tag{7}$$

$$\varepsilon = RT\ln\left(1 + \frac{1}{C_{\mathrm{e}}}\right) \tag{8}$$

$$E = \sqrt{1/2B} \tag{9}$$

First, the Langmuir isotherm (eqn (1)) was applied, assuming a homogeneous adsorbent surface where TC forms a monolayer.[32] With a maximum adsorption capacity (Q_{m}) of 22.84 mg g^{-1}, the highest TC uptake per gram of adsorbent was determined. The Langmuir constant (K_{L}) was found to be 0.5127 L mg^{-1}, reflecting the adsorbent's effectiveness in binding TC. Using eqn (2), the separation factor (R_{L}) was determined to decrease with increasing initial pollutant concentration (C_0), confirming favorable adsorption ($0 < R_{\mathrm{L}} < 1$). With the highest correlation coefficient, the Langmuir isotherm demonstrated the best fit (R^2 = 0.99627) (Fig. 5(a)). To further substantiate the monolayer adsorption nature suggested by the Langmuir model, the standard Gibbs free energy change (ΔG°) was calculated using the equation: $\Delta G^\circ = -RT\ln K_{\mathrm{L}}$ where R is the gas constant (8.314 J mol^{-1} K^{-1}), T is the absolute temperature (in K), and K_{L} is the Langmuir constant (L mol^{-1}). The negative ΔG° values obtained confirm the spontaneous nature of the adsorption process and are consistent with physisorption-dominated monolayer coverage.

The Freundlich isotherm (eqn (3)) was also employed to account for covering a heterogeneous surface with adsorption in a multilayer manner.[33] The Freundlich constant (K_{F}) was calculated as 18.41832 (mg g^{-1}) (L mg^{-1})$^{1/n}$, and the value of $1/n$ was 0.10547, indicating favorable adsorption. The correlation coefficient (R^2) for this model was 0.9707, confirming the adequacy of this isotherm in describing the adsorption process (Fig. 5(b)). The Halsey isotherm (eqn (4)) described multilayer adsorption on heterogeneous surfaces, with the constants n and K calculated as 9.4814 and 9.91×10^{11}, respectively.[34] This model also showed a good fit with R^2 = 0.9707 (Fig. 5(c)). The Harkins–Jura isotherm (eqn (5)) provided insights into multilayer adsorption and pore heterogeneity.[35] The constants A and B were calculated as 1.166×10^5 and 3.13, respectively, with 0.9774 as the correlation coefficient (Fig. 5(d)). The adsorption heat (B_{T}) was determined to be 0.41105 after the interaction energy between the adsorbate and adsorbent was assessed using the Temkin isotherm (eqn (6)). The constant β ($B_{\mathrm{T}} = RT/\beta$), representing the maximum bonding energy, was found to be less than 40 kJ mol^{-1}, at 6.13 kJ mol^{-1}, confirming physical adsorption.[36] The model's correlation coefficient (R^2) was 0.96136 (Fig. 5(e)).

Adsorption takes place on a heterogeneous surface with different site accessibility, according to the Dubinin–Radushkevich (D–R) model, which is consistent with Polanyi's potential theory. The linear expressions of the D–R isotherm are defined using the parameter ε, as shown in eqn (7) and (8). Fig. 5(f) presents the ln qe *versus* ε^2 plot, which was used to extract the parameters B and Q_{s}. A B constant of 216.35 (mol J^{-1})^2 and a saturation adsorption capacity (Q_{s}) of 26.35 mg g^{-1} were determined. It was determined that the mean adsorption energy (E) was 0.048 kJ mol^{-1}, confirming physical adsorption.[37] The D–R model's correlation coefficient (R^2) was 0.94608.

R^2 values were used to fit isotherm models in the following order: Langmuir > Harkins–Jura > Halsey ~ Freundlich > Temkin > D–R. Models such as the Temkin and Harkins–Jura

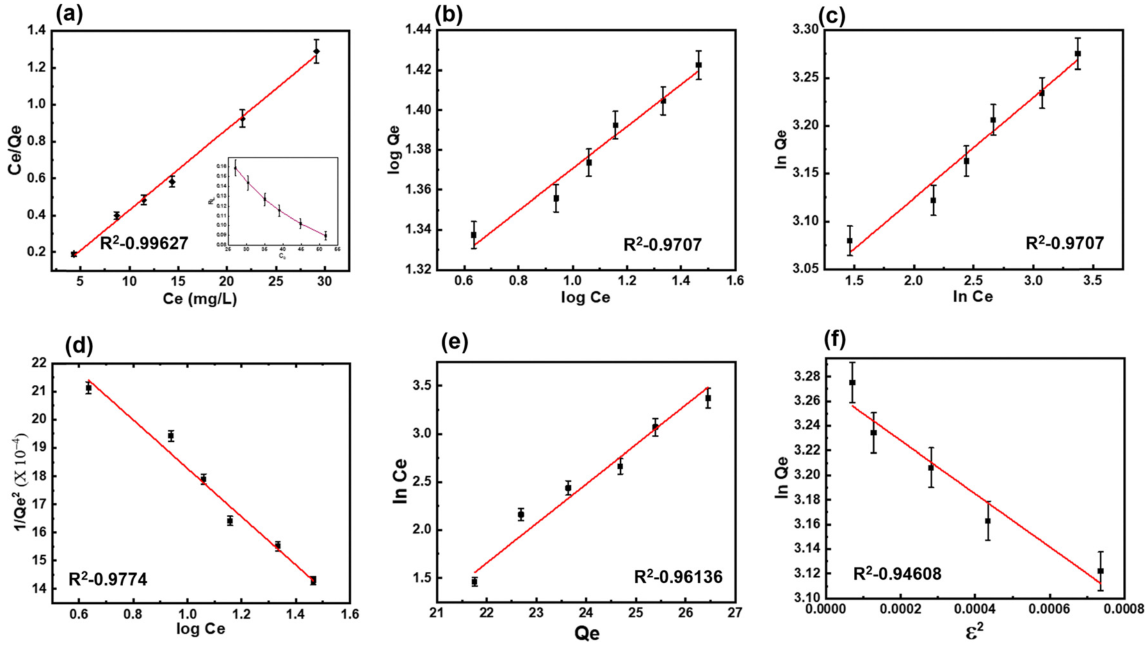

Fig. 5 Plots with linearly fitted adsorption isotherms for (a) Langmuir (inset RL plot), (b) Freundlich, (c) Halsey, (d) Harkins–Jura, (e) Temkin, and (f) D–R models.

exhibited relatively lower correlation coefficients (R^2), suggesting a poorer fit to the experimental data. The Temkin model assumes a linear decrease in the heat of adsorption with increasing surface coverage due to adsorbent–adsorbate interactions, while the Harkins–Jura model is typically suitable for multilayer adsorption on heterogeneous surfaces with high surface heterogeneity. However, in the present system, adsorption appears to be primarily governed by monolayer coverage on energetically uniform sites, as also supported by the better fit of the Langmuir model. Additionally, the weak alignment with these models may be attributed to the limited extent of heat-driven interactions and the presence of mesoporous domains rather than microporous complexity.

The values and parameters of the isotherm are compiled in Table 2.

3.10. Adsorption kinetics

Adsorption kinetics research is necessary to determine the adsorption rate and mechanism, which sheds light on the interaction between the pollutant and the adsorbent. To fully evaluate the adsorption behavior and rate-limiting stages, the experimental kinetic data (Fig. 6(a–e)) were analyzed using a range of models, including pseudo-first-order, pseudo-second-order, Elovich, intraparticle diffusion, and liquid film diffusion models.

One of the oldest and most widely used models for determining the initial rate of adsorption is the pseudo-first-order kinetic model put forth by Lagergren. It is assumed that there is a direct correlation between the quantity of available unoccupied sites and the adsorption rate. The following is the linearized expression for the pseudo-first-order equation:[38]

$$-\ln\left(1-\frac{q_t}{q_e}\right)=k_1 t \tag{10}$$

A linear plot of $\ln(1-q_t/q_e)$ *vs.* time can be used to calculate the slope of the pseudo-first-order rate constant (k_1, min^{-1}). This provides insight into the adsorption kinetics, reflecting how quickly the adsorbate molecules occupy the available adsorption sites.[39]

This is the mathematical equation for the pseudo-second-order kinetic model, which postulates that chemisorption involving electron sharing or exchange between the adsorbent and adsorbate controls the adsorption rate.[40]

$$\frac{t}{q_t}=\frac{1}{k^2 {q_e}^2}+\frac{t}{q_e} \tag{11}$$

The slope and intercept of the linear plot of t/q_t *vs.* t are used to calculate the pseudo-second-order rate constant k_2 (g mg^{-1} min^{-1}), which sheds light on the adsorption mechanism and the interaction between the adsorbent and adsorbate.

The Elovich kinetic model is a highly effective empirical approach for illustrating the energetic heterogeneity of adsorbent surfaces, providing valuable insights into the adsorption mechanism. This model utilizes eqn (12) to validate the occurrence of the chemisorption process, confirming the nature of adsorption interactions.[41]

$$q_t=\frac{1}{\beta}\ln(\alpha\beta)+\frac{1}{\beta}\ln(t) \tag{12}$$

Initially, the adsorption rate is represented by α (mg g^{-1} min^{-1}), while β (g mg^{-1}) correlates with the desorption and chemisorption processes—these parameters, derived from the q_t *versus* $\ln(t)$ plots.

Weber and Morris' intraparticle diffusion model was used to identify the rate-limiting step in TC adsorption onto CH13 by analyzing the experimental adsorption data. This model is represented by eqn (13).[42]

$$q_t=k_1 t^{\frac{1}{2}}+C_1 \tag{13}$$

The intraparticle diffusion rate constant (mg g^{-1} min$^{-0.5}$) is represented by the symbol k_1 in this model. The slope and

Table 2 Parameters of the TC adsorption isotherm on CH13

Equilibrium isotherms models	Equations	Parameters	Values
Langmuir	$\frac{C_e}{q_e}=\frac{1}{Q_m K_L}+\frac{1}{Q_m}C_e$	K_L (L mg^{-1})	0.5127
		Q_m (mg g^{-1})	22.84
		R^2	0.99627
		ΔG° (kJ mol^{-1})	−31.09
Freundlich	$Q_e = K_F {C_e}^{1/n}$	$1/n$	0.10547
		K_F [(mg g^{-1}) (L mg^{-1})$^{1/n}$]	18.41832
		R^2	0.9707
Halsey	$\ln q_e=\frac{1}{n}\ln K-\frac{1}{n}\ln C_e$	n	9.4814
		K	9.91×10^{11}
		R^2	0.9707
Harkins–Jura	$\frac{1}{{q_e}^2}=\left(\frac{B}{A}\right)-\frac{1}{A}\log C_e$	A	1.166×10^5
		B	3.13
		R^2	0.9774
Temkin	$q_e = B_T \ln K_T + B_T \ln C_e$	B_T	0.41105
		K_T (L mg^{-1})	6.3×10^7
		R^2	0.96136
		β (kJ mol^{-1})	6.13
D–R model	$\ln q_e = \ln Qs - B\varepsilon^2$	B [(mol J^{-1})^2]	216.34362
		Q_s (mg g^{-1})	26.3482
		E (kJ mol^{-1})	0.048
		R^2	0.94608

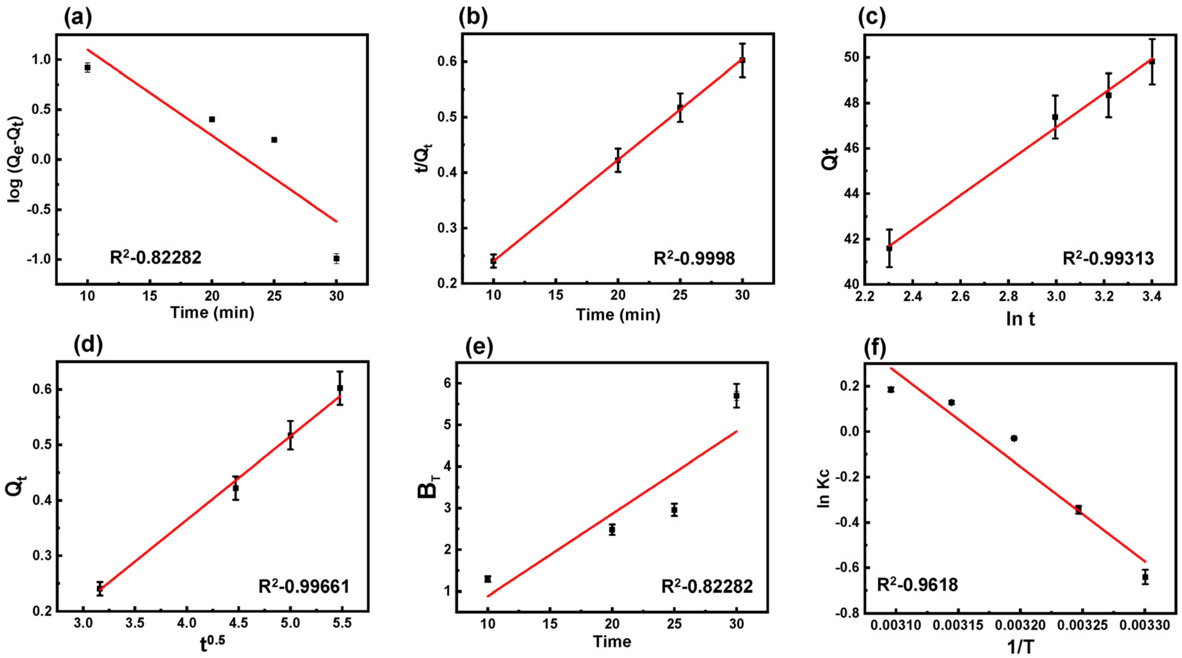

Fig. 6 Plots of kinetic models with linear fits: (a) pseudo-first-order, (b) pseudo-second-order, (c) Elovich model, (d) Intraparticle diffusion model, (e) Liquid film model, and (f) thermodynamic studies.

intercept of the plot of q_t *versus* $t^{0.5}$ are used to get the constants k_1 and C_1.

The liquid film model emphasizes the function of external mass transfer in the overall adsorption mechanism by positing that the diffusion of adsorbate molecules through the boundary layer surrounding the adsorbent mostly controls the adsorption rate.

$$-\ln(1 - F) = k_{fd} \times T \tag{14}$$

Here, K_f stands for the film diffusion constant, and F is the proportion of equilibrium reached, which is expressed as $F = Q_t/Q_e$. The adsorption process is mostly controlled by diffusion through the surrounding liquid film, according to a linear plot of $\ln(1 - F)$ *vs.* time that passes through the origin.

The correlation coefficients and kinetic parameters for all the different kinetic models are compiled in Table 3. Although the experimental data were reasonably fitted by all five models, the pseudo-second-order model offered the best correlation ($R^2 > 0.9997$) for TC adsorption onto CH13. To further validate the reliability of the kinetic model, error bars derived from triplicate measurements were included in the plots. These indicate the variability of adsorption at each time point and confirm the consistency of the kinetic data, supporting the model's robustness. This model assumes that the rate-limiting step involves valency forces, such as electron sharing or exchange, which aligns with the observed results. In comparison, the pseudo-first-order model—more applicable to physisorption—yielded a lower R^2 value. This observation is consistent with Azizian's theory, which posits that adsorption tends to act in a pseudo-second-order manner when the initial concentration of the sorbate falls within a reasonable range. Additionally, surface heterogeneity is indicated by a significant

Table 3 TC's adsorption kinetics characteristics on CH13

Kinetic Models	Equations	Parameters	Values
Pseudo-first-order	$-\ln\left(1-\frac{q_t}{q_e}\right) = k_1 t$	Q_e (mg g^{-1}) k_1 (min^{-1}) R^2	91.1318 0.086 0.82282
Pseudo-second-order	$\frac{t}{q_t} = \frac{1}{k^2 {q_e}^2} + \frac{t}{q_e}$	Q_e (mg g^{-1}) k_2 (min^{-1}) R^2	54.885 0.00569 0.9998
Elovich model	$q_t = \frac{1}{\beta}\ln(\alpha\beta) + \frac{1}{\beta}\ln(t)$	α (mg g^{-1} min^{-1}) β (g mg^{-1}) R^2	194.44 0.1333 0.99313
Intraparticle diffusion	$q_t = k_1 t^{\frac{1}{2}} + C_1$	C_1 (mg g^{-1}) K_1 (min^{-1}) R^2	0.23842 0.15082 0.99661
Liquid-film model	$-\ln(1 - F) = K_{fd} \times T$	K_{fd} R^2	0.19803 0.82282

R^2 for the Elovich model, as there are multiple active sites on the CH13 surface with varying energy levels for adsorption. Also, the Elovich model's good fit indicates the occurrence of chemisorption processes on heterogeneous active sites, which aligns with the complex nature of TC interaction with functionalized surfaces. In contrast, the strong correlation with the intraparticle diffusion hypothesis suggests that adsorption is not restricted to the exterior surface; TC molecules also penetrate into internal pores, indicating a multi-step process involving both surface interaction and diffusion within the adsorbent.

3.11. Thermodynamic studies

Thermodynamic parameters (ΔG°, ΔH°, and ΔS°) provide insights into the spontaneity, heat effects, and molecular behavior of the adsorption mechanism, allowing a deeper understanding of the process and feasibility under different temperatures. These parameters for TC removal using CH13 were found using the van't Hoff equation, which sheds light on the energy changes and spontaneity related to the adsorption mechanism.[43]

$$\ln\left(\frac{q_e}{C_e}\right) = -\frac{\Delta H^\circ}{RT} + \frac{\Delta S^\circ}{R} \tag{15}$$

$$K_c = 1000 \times \frac{q_e}{C_e} \tag{16}$$

$$\ln K_c = \frac{\Delta H^\circ}{RT} + \frac{\Delta S^\circ}{R} \tag{17}$$

Also,

$$\Delta G^\circ = -RT\ln(\rho_w K_D) \tag{18}$$

where ρ_w is the water density (mg L^{-1}) and K_D is the equilibrium constant (L mg^{-1}).

$$\Delta G^\circ = \Delta H^\circ - T(\Delta S^\circ) \tag{19}$$

In this investigation, C_e represents the equilibrium concentration of TC in solution (mg L^{-1}), and q_e represents the quantity of TC adsorbed per gram of CH13 (mg g^{-1}). The absolute temperature is given in Kelvin (K). As seen in Fig. 6(f), thermodynamic parameters including enthalpy change (ΔH°) and entropy change (ΔS°) were computed using the slope and intercept of the van't Hoff plot of $\ln K_c$ *vs.* $1/T$. To ensure dimensionless values for further analysis, the distribution coefficient ($K_d = q_e/C_e$) was converted into K_c by multiplying by 1000 (L g^{-1}).[44] The adsorption process was confirmed to be spontaneous and thermodynamically favorable, as indicated by the negative Gibbs free energy change (ΔG°) at temperatures of 318 K, and 323 K (Table 4). A negative ΔG° indicates that the adsorption of TC onto CH13 is spontaneous and thermodynamically beneficial at the studied temperatures (318 K and 323 K). This means that the process can occur without external energy input. A negative ΔS° signifies a decrease in molecular disturbance at the solid–liquid contact during adsorption. This suggests that TC molecules become more ordered upon binding to the CH13 surface, possibly due to certain interactions like π–π stacking or hydrogen bonding, whereas the process's endothermic nature is confirmed by the positive ΔH°, indicating increased adsorption efficiency at higher temperatures.

Table 4 TC's thermodynamic adsorption parameters on CH13

Temperature (K)	ΔG° (kJ mol^{-1})	ΔH° (kJ mol^{-1})	ΔS° (kJ mol^{-1} K^{-1})	R^2
303	1.614164	34.73423	0.109307	0.9618
308	0.88147		0.109912	
313	0.077176		0.110725	
318	−0.33902		0.110293	
323	−0.49777		0.109077	

3.12. Reusability studies

When employing the composite for long-term environmental remediation, the adsorbent's stability is a crucial consideration. Therefore, it is essential to study the dependability of adsorbent composites throughout multiple adsorption cycles. TC adsorption was carried out six times with the same catalyst for this aim. To desorb TC and make it suitable for reuse, the adsorbent CH13 was centrifuged and cleaned with water and ethanol in between cycles. Removing adsorbed TC molecules from the adsorbent surface is made easier by this washing procedure, which breaks weak connections like hydrogen bonds and van der Waals forces. TC adsorption efficiencies decreased from 94% to 82% (Fig. 7(c)), and the CH13 composite remained exceptionally stable even after six cycles. The removal efficiency dropped from 94% to 82%, most likely as a result of several catalysts being lost during the recovery process. Additionally, during repeated cycles, untreated molecules may stick to the adsorbent CH13's surface, obstructing pores and active sites and perhaps reducing performance. The XRD analysis showed a modest decrease in peak intensity after six cycles, indicating that some TC molecules adhered to the adsorbent's surface. However, the overall XRD pattern remained largely unchanged, which suggests that the CH13 composite maintained its structural stability and didn't experience notable degradation. Nevertheless, the CH13's XRD pattern remained consistent, indicating its structural stability, as seen in Fig. 7(a). While these findings demonstrate material robustness, a more holistic assessment—particularly for scale-up applications—requires consideration of regeneration costs and energy consumption. Although such economic analyses were beyond the scope of the present study, it is important to note that CH13 was synthesized using halloysite clay, a naturally abundant and low-cost material. This not only imparts structural support but also enhances the affordability and sustainability of the composite relative to purely CP-based systems to better evaluate the feasibility of CH13 for real-world environmental applications.

3.13. Adsorption mechanism

There are a number of mechanisms that can be used to explain adsorption processes, such as metal–ligand coordination, π–π interactions, pore filling, hydrogen bonding, and van der Waals forces.[22,45] The adsorption mechanism of TC onto the

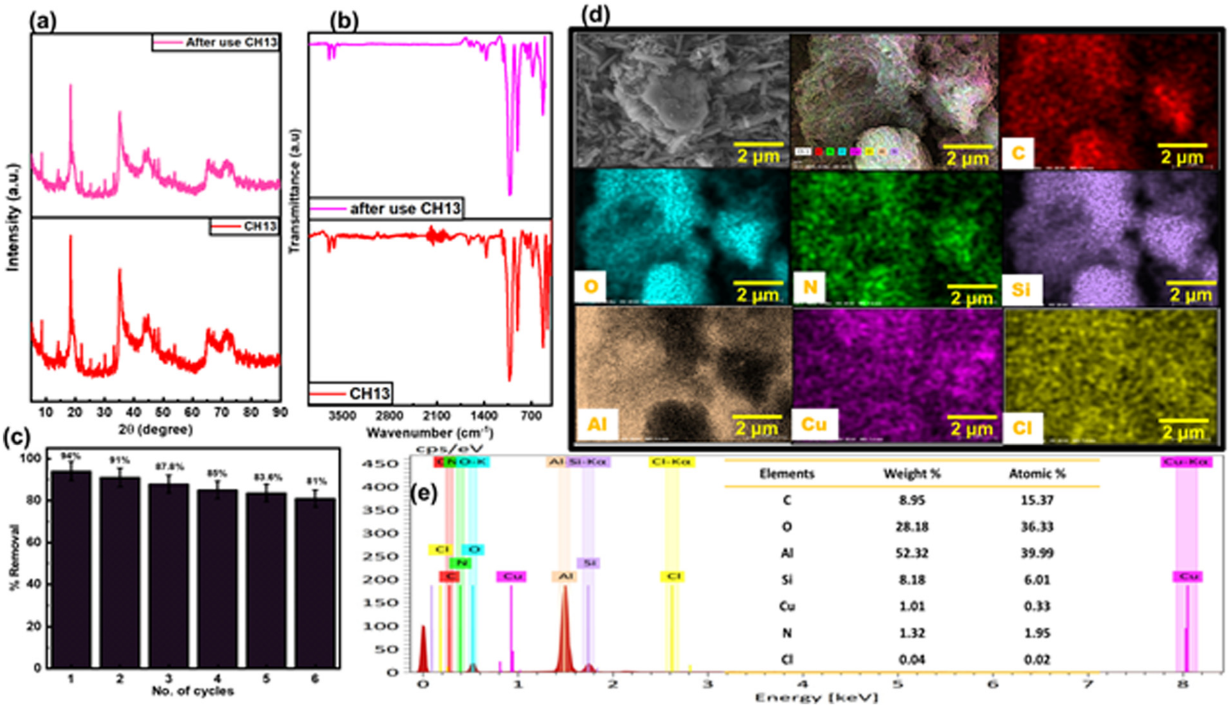

Elements	Weight %	Atomic %
C	8.95	15.37
O	28.18	36.33
Al	52.32	39.99
Si	8.18	6.01
Cu	1.01	0.33
N	1.32	1.95
Cl	0.04	0.02

Fig. 7 (a) XRD plot, (b) FTIR spectra, (c) reusability cycles, (d) FESEM image and elemental colour mapping, and (e) EDS analysis after adsorption of TC onto CH13.

CH13 composite can be comprehensively understood through post-adsorption FTIR, XRD, FESEM, and EDS analyses. Based on the adsorption data, hydrogen bonding is crucial to the elimination process because the hydroxyl and carboxyl groups on the CH13 composite create robust bonds with the TC's polar functional groups. This interaction helps anchor the adsorption process by attracting TC molecules to the composite surface as evidenced by FTIR spectra (Fig. 7(b)), where the

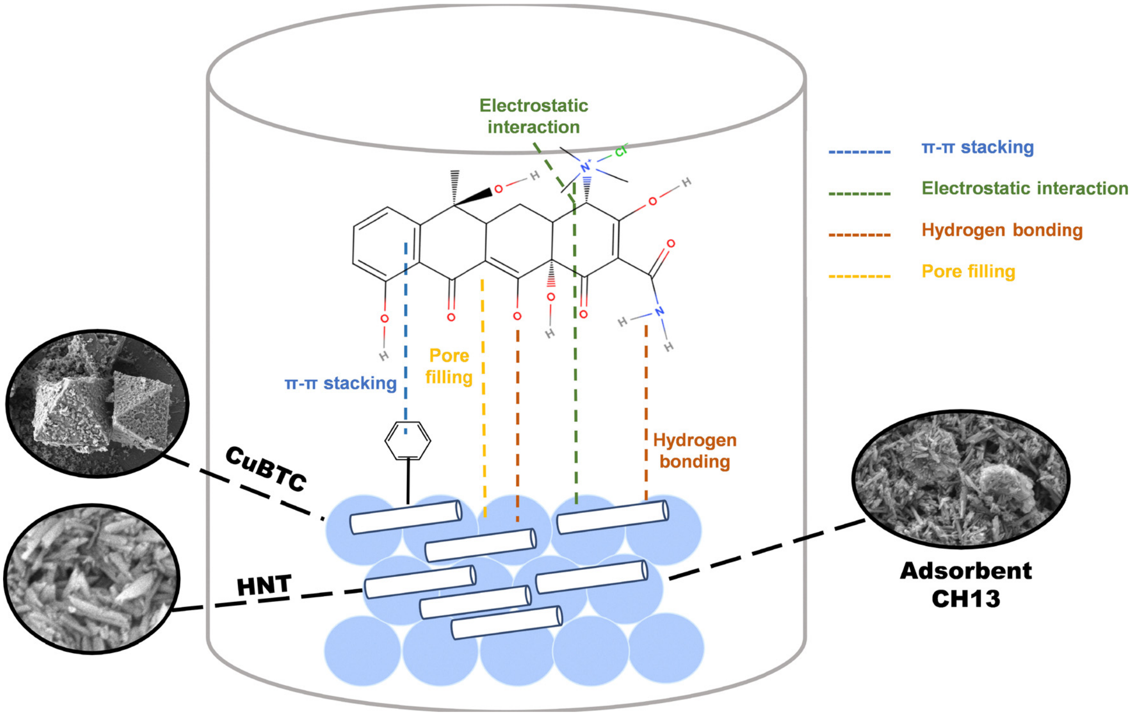

Scheme 2 Adsorption scheme of TC onto CH13.

characteristic –OH stretching vibration of CH13 is weakened and shifted after adsorption. The polar functional groups of TC and the hydroxyl and carboxyl groups on the composite surface establish robust hydrogen bonding, thereby improving the adsorption efficiency. Additionally, π–π interactions contribute significantly to the stability of the adsorption by enhancing the affinity of TC for the composite surface, leading to more efficient removal. Electrostatic interactions further govern the adsorption, particularly within the pH range of 5–10. At higher pH, TC predominantly exists in its deprotonated form, increasing its attraction to the positively charged sites of CH13. Additionally, metal–ligand coordination between Cu^{2+} centers in CB and oxygen/nitrogen atoms in TC further stabilizes the adsorption by forming additional bonds from TC's functional groups to its metal centers. The high porosity of CH13 facilitates pore filling, allowing TC molecules to be efficiently trapped within the composite structure. FESEM and EDS analyses (Fig. 7(d and e)) show an increase in surface roughness and irregularity of the CH13 composite post-adsorption, indicating that TC molecules have been effectively trapped on the surface. Elemental mapping further confirms the presence of TC on the composite, supporting the conclusion that adsorption has occurred. The BET surface area was evaluated using the N_2 adsorption–desorption isotherm. After adsorption, the surface area decreased notably from 154.9 to 21.8 $m^2\ g^{-1}$, while the total pore volume declined from 0.1991 to 0.0591 $cm^3\ g^{-1}$. This reduction reflects the effective occupation of the composite's pores by tetracycline molecules. Such textural changes support the high adsorption capacity observed and suggest that the adsorbent's porous structure was efficiently exploited during the removal process. Hence, all these interactions support the adsorption of TC onto CH13 as shown in Scheme 2.

3.14. Comparison table for various adsorbents

Table S1 (ESI†) compares the TC removal efficiency of the synthesized CH13 with other adsorbents found in the literature.

4. Conclusion

This study successfully developed a novel CuBTC–HNT composite through a sustainable hydrothermal approach, optimizing its structure for effective antibiotic removal from wastewater. The formation and structural stability of CuBTC, HNT, and their composites were rigorously confirmed using a variety of characterization methods, demonstrating their large surface area, unique porosity, and resistance to heat. Adsorbent dosage, pH, beginning TC concentration, agitation speed, temperature, and contact time were all optimized in order to thoroughly evaluate these materials' adsorption performance. The synergistic interaction between CuBTC and HNT significantly enhanced the adsorption capacity, with the optimized composite achieving an impressive TC removal efficiency of 94% for a 25 ppm solution from pH 5–10, 50 °C, and 800 rpm within 35 minutes. Isotherm studies demonstrated that the adsorption behavior followed the Langmuir model ($R^2 = 0.99627$), showing a uniform surface with monolayer adsorption. According to kinetic modeling, the pseudo-second-order model ($R^2 = 0.9998$), which had a rate constant of 0.00569 min^{-1}, best explained the adsorption mechanism, suggesting chemisorption as the dominant process. The thermodynamic analysis further reinforced this conclusion, verifying the process's endothermic and spontaneous character ($\Delta H = 34.73423$ kJ mol^{-1}, $\Delta G = -0.49777$ kJ mol^{-1}, and $\Delta S = 0.109077$ kJ mol^{-1} K^{-1}). The reusability studies indicated that the material retained its adsorption efficiency over six consecutive cycles, with only a minimal decrease, attributed to slight catalyst loss and partial pore obstruction. However, XRD analysis confirmed that the composite maintained its structural integrity after multiple adsorption–desorption cycles. Overall, this research establishes the CuBTC–HNT composite as a highly efficient, reusable, and scalable adsorbent for the long-term elimination of TC from polluted water. Its superior adsorption removal, rapid kinetics, and long-term stability position it as a promising material for addressing the critical environmental challenge posed by pharmaceutical pollutants in aquatic systems.

Author contributions

Palkaran: designed and performed the experiments, analyzed data, and co-wrote the paper. Sanghamitra Barman: supervised the research, designed experiments, and co-wrote the paper. Soumen Basu: supervised the research, designed experiments, and co-wrote the paper.

Conflicts of interest

The authors declare that they have no known competing financial interests or personal relationships that could have appeared to influence the work reported in this paper.

Data availability

The data supporting the findings of this study, including characterization results, adsorption and degradation kinetics, and isotherm studies, are available in the article as well as in the ESI† provided with this article.

Acknowledgements

The authors would like to acknowledge Thapar Institute of Engineering and Technology for XRD, FESEM, and FTIR. The authors are also grateful to IIT Roorkee for XPS and Panjab University, Chandigarh, for HRTEM analysis.

References

1 S. Gai, J. Zhang, R. Fan, K. Xing, W. Chen, K. Zhu, X. Zheng, P. Wang, X. Fang and Y. Yang, Highly Stable Zinc-Based Metal–Organic Frameworks and Corresponding Flexible Composites for Removal and Detection of Antibiotics in

Water, *ACS Appl. Mater. Interfaces*, 2020, **12**(7), 8650–8662, DOI: 10.1021/acsami.9b19583.

2 Md Imran, K. R. Das and M. M. Naik, Co-Selection of Multi-Antibiotic Resistance in Bacterial Pathogens in Metal and Microplastic Contaminated Environments: An Emerging Health Threat, *Chemosphere*, 2019, **215**, 846–857, DOI: 10.1016/j.chemosphere.2018.10.114.

3 Y. Zhu, K. Liu, J. Zhang, X. Liu, L. Yang, R. Wei, S. Wang, D. Zhang, S. Xie and F. Tao, Antibiotic Body Burden of Elderly Chinese Population and Health Risk Assessment: A Human Biomonitoring-Based Study, *Environ. Pollut.*, 2020, **256**, 113311, DOI: 10.1016/j.envpol.2019.113311.

4 X.-D. Zhu, Y.-J. Wang, R.-J. Sun and D.-M. Zhou, Photocatalytic Degradation of Tetracycline in Aqueous Solution by Nanosized TiO2, *Chemosphere*, 2013, **92**(8), 925–932, DOI: 10.1016/j.chemosphere.2013.02.066.

5 D. Li, M. Yang, J. Hu, Y. Zhang, H. Chang and F. Jin, Determination of Penicillin G and Its Degradation Products in a Penicillin Production Wastewater Treatment Plant and the Receiving River, *Water Res.*, 2008, **42**(1), 307–317, DOI: 10.1016/j.watres.2007.07.016.

6 M. G. Antoniou, A. A. de la Cruz and D. D. Dionysiou, Degradation of Microcystin-LR Using Sulfate Radicals Generated through Photolysis, Thermolysis and E− Transfer Mechanisms, *Appl. Catal., B*, 2010, **96**(3), 290–298, DOI: 10.1016/j.apcatb.2010.02.013.

7 C. V. Gómez-Pacheco, M. Sánchez-Polo, J. Rivera-Utrilla and J. López-Peñalver, Tetracycline Removal from Waters by Integrated Technologies Based on Ozonation and Biodegradation, *Chem. Eng. J.*, 2011, **178**, 115–121, DOI: 10.1016/j.cej.2011.10.023.

8 M. F. Mubarak, H. Selim, H. B. Hawash and M. Hemdan, Flexible, Durable, and Anti-Fouling Maghemite Copper Oxide Nanocomposite-Based Membrane with Ultra-High Flux and Efficiency for Oil-in-Water Emulsions Separation, *Environ. Sci. Pollut. Res.*, 2024, **31**(2), 2297–2313, DOI: 10.1007/s11356-023-31240-x.

9 Y. Liu, X. Fan, X. Jia, X. Chen, A. Zhang, B. Zhang and Q. Zhang, Preparation of Magnetic Hyper-Cross-Linked Polymers for the Efficient Removal of Antibiotics from Water, *ACS Sustainable Chem. Eng.*, 2018, **6**(1), 210–222, DOI: 10.1021/acssuschemeng.7b02252.

10 K. Althumayri, A. Guesmi, W. Abd El-Fattah, L. Khezami, T. Soltani, N. Hamadi, A. Ben and A. Shahat, Effective Adsorption and Removal of Doxorubicin from Aqueous Solutions Using Mesostructured Silica Nanospheres: Box–Behnken Design Optimization and Adsorption Performance Evaluation, *ACS Omega*, 2023, **8**(15), 14144–14159, DOI: 10.1021/acsomega.3c00829.

11 G. O. El-Sayed, M. M. Yehia and A. A. Asaad, Assessment of Activated Carbon Prepared from Corncob by Chemical Activation with Phosphoric Acid, *Water Resour. Ind.*, 2014, **7–8**, 66–75, DOI: 10.1016/j.wri.2014.10.001.

12 G. Crini and E. Lichtfouse, Advantages and Disadvantages of Techniques Used for Wastewater Treatment, *Environ. Chem. Lett.*, 2019, **17**(1), 145–155, DOI: 10.1007/s10311-018-0785-9.

13 W. Hu, S. Wang, C. Jiang, M. Zheng, Z. Bai, D. Srivastava, A. Kumar and J. Liu, Recent Advances in Sonodynamic Therapy by MOFs-Based Platforms for Biomedical Applications, *Dyes Pigm.*, 2023, **219**, 111596, DOI: 10.1016/j.dyepig.2023.111596.

14 P. Sethi, S. Basu and S. Barman, Innovative CuBTC/g-C3N4 Materials for Tetracycline Mitigation: Adsorption, Photocatalysis, and Mechanistic Perspectives, *New J. Chem.*, 2025, **49**(20), 8454–8471, DOI: 10.1039/d5nj00556f.

15 P. Sethi, S. Barman and S. Basu, Strategic Tuning of GO Ratios in CuBTC-GO Nanocomposites for next-Generation Tetracycline Adsorption: A Deep Dive into Isotherms, Kinetics, and Thermodynamics, *Sep. Purif. Technol.*, 2025, **361**, 131311, DOI: 10.1016/j.seppur.2024.131311.

16 S. Yakkerimath, R. M. Kulkarni, S. V. Divekar, V. R. Chate and K. Purandara Bekal, Kinetic, Adsorption, and Thermodynamic Study of Removal of Cr6+ by Iron-Rich Natural Clay Minerals, *Desalination Water Treat.*, 2024, **318**, 100302, DOI: 10.1016/j.dwt.2024.100302.

17 H. Shekhawat, A. Kumari, H. Raol and T. Choudhury, Preparation and Characterization of Clay Hybrid Adsorbents for the Removal of Paracetamol from Model Wastewater: A Comparative Study, *Appl. Clay Sci.*, 2024, **258**, 107469, DOI: 10.1016/j.clay.2024.107469.

18 F. Bessaha, N. Mahrez, K. Marouf-Khelifa, A. Çoruh and A. Khelifa, Removal of Congo Red by Thermally and Chemically Modified Halloysite: Equilibrium, FTIR Spectroscopy, and Mechanism Studies, *Int. J. Environ. Sci. Technol.*, 2019, **16**(8), 4253–4260, DOI: 10.1007/s13762-018-2041-z.

19 G. Bessaha, F. Bessaha, N. Mahrez, F. Boucif, A. Çoruh and A. Khelifa, Enhancement of the Comprehensive Performance of Tetracycline Adsorption by Halloysite Nanotubes: Kinetics, Mechanism, and Reusability Study, *Desalination Water Treat.*, 2024, **320**, 100695, DOI: 10.1016/j.dwt.2024.100695.

20 N. Wang, W. Ma, Y. Hou and H. Gao, Examining the Adsorption Efficiency of Iron Oxide-Decorated Magnetic Halloysite Nanotubes for Tetracycline Elimination from Solutions, *Mater. Res. Express*, 2023, **10**(12), 125001, DOI: 10.1088/2053-1591/ad1074.

21 Q. Wang, M. Yang, X. Qi, J. Wang, K. Sun, Z. Li and G. Deng, A Novel Graphene Oxide Decorated with Halloysite Nanotubes (HNTs/GO) Composite Used for the Removal of Levofloxacin and Ciprofloxacin in a Wide PH Range, *New J. Chem.*, 2021, **45**(39), 18315–18326, DOI: 10.1039/D1NJ03807A.

22 B. Garg, P. Sethi and S. Basu, Strategic Innovation in CuBTC/PANI Nanocomposites for Dye Remediation: A Holistic Approach for Enhancing Adsorption, Isotherms, and Kinetic Studies, *RSC Sustainability*, 2025, **3**(5), 2311–2324, DOI: 10.1039/d5su00056d.

23 M. S. Samuel, K. V. Savunthari and S. Ethiraj, Synthesis of a Copper (II) Metal–Organic Framework for Photocatalytic Degradation of Rhodamine B Dye in Water, *Environ. Sci. Pollut. Res.*, 2021, **28**(30), 40835–40843, DOI: 10.1007/s11356-021-13571-9.

24 A. Garg, S. Basu, R. L. Mahajan and R. Mehta, Enhancement in Mechanical Properties of GFRP-Coal-Derived Graphene Oxide Composites by Addition of Multiwalled Carbon Nanotubes and Halloysite Nanotubes: A Comparative Study, *Polym. Compos.*, 2024, **45**(14), 13164–13179, DOI: **10.1002/pc.28694**.

25 V. Jabbari, J. M. Veleta, M. Zarei-Chaleshtori, J. Gardea-Torresdey and D. Villagrán, Green Synthesis of Magnetic MOF@GO and MOF@CNT Hybrid Nanocomposites with High Adsorption Capacity towards Organic Pollutants, *Chem. Eng. J.*, 2016, **304**, 774–783, DOI: **10.1016/j.cej.2016.06.034**.

26 R. Bardestani, G. S. Patience and S. Kaliaguine, Experimental Methods in Chemical Engineering: Specific Surface Area and Pore Size Distribution Measurements—BET, BJH, and DFT, *Can. J. Chem. Eng.*, 2019, **97**(11), 2781–2791, DOI: **10.1002/cjce.23632**.

27 H. Niu, S. Liu, Y. Cai, F. Wu and X. Zhao, MOF Derived Porous Carbon Supported Cu/Cu2O Composite as High Performance Non-Noble Catalyst, *Microporous Mesoporous Mater.*, 2016, **219**, 48–53, DOI: **10.1016/j.micromeso.2015.07.027**.

28 R. Al-Gaashani, Y. Zakaria, I. Gladich, V. Kochkodan and J. Lawler, XPS, Structural and Antimicrobial Studies of Novel Functionalized Halloysite Nanotubes, *Sci. Rep.*, 2022, **12**(1), 21633, DOI: **10.1038/s41598-022-25270-7**.

29 S. S. Gabr, M. F. Mubarak, M. Keshawy, I. E. T. El Sayed and T. Abdel Moghny, Linear and Nonlinear Regression Analysis of Phenol and P-Nitrophenol Adsorption on a Hybrid Nanocarbon of ACTF: Kinetics, Isotherm, and Thermodynamic Modeling, *Appl. Water. Sci.*, 2023, **13**(12), 230, DOI: **10.1007/s13201-023-02018-w**.

30 S. Singla, P. Devi and S. Basu, Highly Effectual Photocatalytic Remediation of Tetracycline under the Broad Spectrum of Sunlight by Novel BiVO4/Sb2S3 Nanocomposite, *Catalysts*, 2023, **13**(4), 731, DOI: **10.3390/catal13040731**.

31 B. Garg, P. Hait and S. Basu, Unlocking Solar Energy's Potential: Dual Photocatalytic Activities of g-C3N4/Sb2S3 for Hydrogen Evolution and Tetracycline Degradation in Sunlight, *J. Environ. Manage.*, 2024, **370**, 122403, DOI: **10.1016/j.jenvman.2024.122403**.

32 N. Mukwevho, R. Gusain, E. Fosso-Kankeu, N. Kumar, F. Waanders and S. S. Ray, Removal of Naphthalene from Simulated Wastewater through Adsorption-Photodegradation by ZnO/Ag/GO Nanocomposite, *J. Ind. Eng. Chem.*, 2020, **81**, 393–404, DOI: **10.1016/j.jiec.2019.09.030**.

33 N. Ghasemi, M. Ghasemi, S. Moazeni, P. Ghasemi, N. S. Alharbi, V. K. Gupta, S. Agarwal, I. V. Burakova and A. G. Tkachev, Zn (II) Removal by Amino-Functionalized Magnetic Nanoparticles: Kinetics, Isotherm, and Thermodynamic Aspects of Adsorption, *J. Ind. Eng. Chem.*, 2018, **62**, 302–310, DOI: **10.1016/j.jiec.2018.01.008**.

34 N. Goyal, V. K. Bulasara and S. Barman, Removal of Emerging Contaminants Daidzein and Coumestrol from Water by Nanozeolite Beta Modified with Tetrasubstituted Ammonium Cation, *J. Hazard. Mater.*, 2018, **344**, 417–430, DOI: **10.1016/j.jhazmat.2017.10.051**.

35 N. Goyal, S. Barman and V. K. Bulasara, Efficient Removal of Bisphenol S from Aqueous Solution by Synthesized Nano-Zeolite Secony Mobil-5, *Microporous Mesoporous Mater.*, 2018, **259**, 184–194, DOI: **10.1016/j.micromeso.2017.10.015**.

36 A. Garg, M. Mainrai, V. K. Bulasara and S. Barman, Experimental investigation on adsorption of amido black 10b dye onto zeolite synthesized from fly ash, *Chem. Eng. Commun.*, 2015, **202**(1), 123–130, DOI: **10.1080/00986445.2013.836636**.

37 N. Wang, J. Chen, J. Wang, J. Feng and W. Yan, Removal of Methylene Blue by Polyaniline/TiO2 Hydrate: Adsorption Kinetic, Isotherm and Mechanism Studies, *Powder Technol.*, 2019, **347**, 93–102, DOI: **10.1016/j.powtec.2019.02.049**.

38 A. K. Ojha and V. K. Bulasara, Adsorption Characteristics of Jackfruit Leaf Powder for the Removal of Amido Black 10B Dye, *Environ. Prog. Sustainable Energy*, 2015, **34**(2), 461–470, DOI: **10.1002/ep.12015**.

39 Y. S. Ho and G. McKay, Pseudo-Second Order Model for Sorption Processes, *Process Biochem.*, 1999, **34**(5), 451–465, DOI: **10.1016/S0032-9592(98)00112-5**.

40 W. Yuanfeng, Z. Lei, M. Jianwei, L. Shiwang, H. Jun, Y. Yuru and M. Lehe, Kinetic and Thermodynamic Studies of Sulforaphane Adsorption on Macroporous Resin, *J. Chromatogr. B: Anal. Technol. Biomed. Life Sci.*, 2016, **1028**, 231–236, DOI: **10.1016/j.jchromb.2016.06.035**.

41 A. P. Vieira, S. A. A. Santana, C. W. B. Bezerra, H. A. S. Silva, J. A. P. Chaves, J. C. P. Melo, E. C. S. Filho and C. Airoldi, Removal of Textile Dyes from Aqueous Solution by Babassu Coconut Epicarp (Orbignya Speciosa), *Chem. Eng. J.*, 2011, **173**(2), 334–340, DOI: **10.1016/j.cej.2011.07.043**.

42 S. Agarwal, I. Tyagi, V. Gupta, N. Ghasemi, M. Shahivand and M. Ghasemi, Kinetics, Equilibrium Studies and Thermodynamics of Methylene Blue Adsorption on Ephedra Strobilacea Saw Dust and Modified Using Phosphoric Acid and Zinc Chloride, *J. Mol. Liq.*, 2016, **218**, 208–218, DOI: **10.1016/j.molliq.2016.02.073**.

43 J. Sharma, M. Sharma and S. Basu, Synthesis of Mesoporous MgO Nanostructures Using Mixed Surfactants Template for Enhanced Adsorption and Antimicrobial Activity, *J. Environ. Chem. Eng.*, 2017, 5(4), 3429–3438, DOI: **10.1016/j.jece.2017.07.015**.

44 A. Khadir, M. Motamedi, M. Negarestani, M. Sillanpää and M. Sasani, Preparation of a Nano Bio-Composite Based on Cellulosic Biomass and Conducting Polymeric Nanoparticles for Ibuprofen Removal: Kinetics, Isotherms, and Energy Site Distribution, *Int. J. Biol. Macromol.*, 2020, **162**, 663–677, DOI: **10.1016/j.ijbiomac.2020.06.095**.

45 S. S. Kahu, A. Shekhawat, D. Saravanan and R. M. Jugade, Two Fold Modified Chitosan for Enhanced Adsorption of Hexavalent Chromium from Simulated Wastewater and Industrial Effluents, *Carbohydr. Polym.*, 2016, **146**, 264–273, DOI: **10.1016/j.carbpol.2016.03.041**.